Article

Another Potentially Hazardous Zeolite from Northern Italy: Fibrous Mordenite

Matteo Giordani [1],* [iD]**, Paolo Ballirano [2]** [iD]**, Alessandro Pacella [2]** [iD]**, Maria Assunta Meli [3], Carla Roselli [3], Fulvio Di Lorenzo [4], Ivan Fagiolino [5] and Michele Mattioli [1]** [iD]

[1] Department of Pure and Applied Sciences, University of Urbino Carlo Bo, 61029 Urbino, Italy; michele.mattioli@uniurb.it

[2] Department of Earth Sciences, Sapienza University of Rome, 00185 Rome, Italy; paolo.ballirano@uniroma1.it (P.B.); alessandro.pacella@uniroma1.it (A.P.)

[3] Department of Biomolecular Sciences, University of Urbino Carlo Bo, 61029 Urbino, Italy; maria.meli@uniurb.it (M.A.M.); carla.roselli@uniurb.it (C.R.)

[4] Laboratory for Waste Management, Paul Scherrer Institute, 5232 Villigen, Switzerland; fulvio.dilorenzo@psi.ch

[5] Gruppo C.S.A. SpA, 47923 Rimini, Italy; ifagiolino@csaricerche.com

* Correspondence: matteo.giordani@uniurb.it

Abstract: This study explored morphological, mineralogical, and physicochemical features of suspected toxic mordenite fibers from Northern Italy. All the mordenite samples (FAS1, GC1, SP1) show similar structural and chemical character, are Na-rich (Na > Ca > K), and the Al content decrease reflects the unit cell volumes in the series: FAS1 > SP1 > GC1. The aerodynamic diameter (D_{ae}) values of the mordenite fibers are 1.19 µm for the GC1 sample, 2.69 µm for FAS1, and 3.91 µm for SP1. All the studied mordenite samples are characterized by "respirable" fibers despite the size differences, which could reach the deeper parts of the lungs. For this reason, fibrous mordenite could represent a potential health hazard and then need to be handled with attention, but further toxicity studies are needed.

Keywords: fibrous zeolites; mineral fibers; health hazard; fibrous mordenite; Northern Italy

1. Introduction

Mordenite is an aluminosilicate mineral belonging to the zeolite group. The origin of the name comes from Morden County, Nova Scotia, Canada, where this fibrous mineral in radial aggregate was observed for the first time by How [1]. The ideal chemical formula of mordenite is $(Na_2,K_2,Ca)_4[Al_8Si_{40}O_{96}]\cdot 28H_2O$ and cell parameters are: a = 18.05–18.25 Å, b = 20.35–20.53 Å, c = 7.49–7.55 Å, Z = 1 [2,3].

Mordenite (MOR framework-type) [4] is characterized by puckered sheets consisting of six-membered rings parallel to (100), linked by four-membered rings. This structural arrangement produces strongly compressed eight-member (8MRc: 5.7 × 2.5 Å) and ellipsoidal twelve-member channels (12MRc: 7.0 × 6.5 Å) extending along c. Those channels intersect with less-compressed eight-member channels running along b (8MRb: 4.8 × 3.4 Å), forming a peculiar "plumbing system" accessible for extra-framework cation and molecule diffusion [5]. The framework density, FD, is 17.2 T/1000 Å^3 and the average R, Ra = Si/(Si+Al) is 0.83 [3,4,6]. The structure of mordenite was solved by Meier [7] in the *Cmcm* space group. However, this symmetry leads to an unfavorable T–O–T angle of 180°. Subsequently, a symmetry lowering to the acentric *Cmc2$_1$* space group provided a more accurate description of the extra-framework cation and H_2O molecule population, concurrently preventing the occurrence of the energetically unfavorable T–O–T angle of 180° [8]. It is worth noting that Alberti et al., [8] and Simoncic and Armbruster [5], constrained couples of pseudo-centrosymmetric framework atoms to freely move but maintaining the coordinates related by the inversion center, imposing, *de facto*, a *Cmcm* symmetry to the framework. In

addition, framework defects have been consistently reported, as testified by the occurrence of diffuse scattering in electron diffraction photographs or reconstruction of reciprocal layers from area detector measurement from synchrotron radiation diffraction experiments (see, for example, Simoncic and Armbruster [5]).

Mordenite has been described in vugs of basalts and other volcanic rocks and intrusive (granite) rocks, and as a diagenetic product of silicic tuff, pitchstone, and volcanic sediments [3]. Red compact masses of mordenite with radial and fibrous habits were often observed in amygdaloidal samples, associated with quartz, hematite, and other zeolites such as analcime, chabazite, heulandite, dachiardite, stilbite, natrolite, scolecite, epistilbite, ferrierite, erionite, and thomsonite. In diagenetically altered volcanic sediments, mordenite generally occurs in association with clinoptilolite, chabazite, erionite, phillipsite, ferrierite, and analcime [2,3]. Occurrences of mordenite are common worldwide, but generally its content in diagenetic deposits is higher than in hydrothermal ones. However, in both cases, mordenite occurs with the fibrous habit [3,9].

In Italy, mordenite has been described in some localities of Sardinia [2,10,11], in the Island of Elba [2,8], in the Island of Ponza [12], and many localities from Northern Italy [2,13,14]. Except for Ponza mordenite, which has a diagenetic origin, all the mordenite crystals from Italy were originated in basaltic vugs.

In Northern Italy, mordenite is common in Lessini Mounts (Vicenza) and Fassa Valley (Trento), and it usually occurs in compact masses of fibers with a radiated habit, associated with microcrystalline quartz, hematite, and calcite [2,14]. In the Lessini Mounts, tertiary magmatic products of the Veneto Volcanic Province range from poorly to highly vesiculated basalts and basanites [15]. Basalt vesicles are often filled with secondary minerals of hydrothermal origin, especially zeolites (analcime, chabazite, phillipsite, harmotome, gmelinite, yugawaralite, and willhendersonite [16–19]). Moreover, other fibrous zeolites (erionite, offretite, and ferrierite) have been recently discovered in several localities of Lessini Mounts: these findings are of particular importance due to their toxicological implications [20–24]. Furthermore, in the Dolomites area (where Fassa Valley is located), a great amount of volcanic material is present. Here, volcanic and plutonic products of the magmatic series of Middle Triassic rocks are widespread, occurring as pyroclastic layers, reworked volcaniclastics, pillow lavas, pillow breccias, and hyaloclastics [25,26]. The vugs of these volcanic rocks are widely zeolitized, and several species are present, in particular analcime, natrolite, thomsonite, heulandite, clinoptilolite, chabasite, mordenite, dachiardite, and laumontite [14,27].

Zeolites are widely used in many fields, such as agronomy and ecology, in many industrial processes such as the production of detergents and drying agents, and in medicine [3,28–30]. In particular, mordenite is a very used zeolite because of its high silica/alumina ratio, which allows it to resist exposure to high temperatures and acids, either gaseous or liquids [31,32]. Mordenite is widely used both in natural and synthetic form, especially in the petrochemical industry, as a catalyst in industrial processes, as a host matrix in semiconductors, chemical sensors, and as a selective membrane for adsorptive separation of gas or liquid mixtures [31–36].

Despite the number of industrial applications of mordenite and its physicochemical similarities to the carcinogen fibrous erionite, there are very few studies on the hazard of mordenite involving animals [37–41] or cell lines [42,43]. Moreover, sometimes the tested mordenite was not fibrous, contained more than 50% of other mineral phases or the proportion of fibers in the material was not specified, the experiment duration was short, small numbers of animals were tested, and information on survival was lack, as highlighted by Guthrie and IARC [44,45]. For this reason, mordenite is classified as Group 3 by IARC but detailed research is needed, as suggested by the recent literature. In recent decades, some studies focused on the possibility that mordenite could be a potential inhalation health hazard [46,47]. In general, the available information indicates that the health risk associated with mordenite is low or null, especially if compared to erionite [44]. Erionite and mordenite show different cytotoxic capabilities. Mordenite resulted not mutagenic and

the presence of ferrous ion in the crystals did not alter mordenite's mutagenic potential [43]. Many other fibrous zeolites such as erionite [48–50], offretite [23,51], ferrierite [24,52,53], mesolite, and thomsonite [54] resulted in different toxicity and carcinogenicity response to humans.

The most important factors related to toxicity and carcinogenicity of the fibers are the size parameters (length, diameter, aerodynamic diameter), chemical composition and related bio-persistence, and other features (e.g., microtopography, surface area, structure, net charge, zeta potential, interacting capability, impurities, and toxic elements) [48,55–65].

Due to the abundance of mordenite in some volcanic rocks of Northern Italy and its suspected toxicity to humans, an accurate characterization of these fibers is of paramount importance. In the present work, a detailed morphological, chemical, and structural characterization of different mordenite samples from Northern Italy is presented. Data from Scanning Electron Microscopy with Energy Dispersive X-ray (SEM-EDX), Electron MicroProbe Analysis (EMPA), X-ray Powder Diffraction (XRPD), Thermo Gravimetric Analysis-Differential Scanning Calorimetry (TGA-DSC), and Inductively Coupled Plasma Atomic Emission Spectroscopy (ICP-AES) were combined to characterize from the morphological, chemical, and structural point of view this zeolite. Particular attention was paid to the small fibers detected on the investigated samples.

2. Materials and Methods

2.1. Material

In the present work, three mordenite samples from Northern Italy were investigated. Two samples are from Val Duron (FAS1) and Do' Le Pale (GC1), Fassa Valley, Trentino-Alto Adige. The third sample (SP1) is from Torrebelvicino, Zuccanti Valley, Lessini Mounts, Veneto Region.

2.2. Morphological Analysis

Morphological analysis was performed using an Environmental Scanning Electron Microscope (ESEM) FEI Quanta 200 FEG (FEI, Hillsboro, OR, USA). The operating conditions were 30 kV accelerating voltage, 10 mm working distance, 0 tilt angle, and variable beam diameter. The images were collected with a back-scattered electron detector. Morphometric data were collected by accurate fiber size measurements (length and diameter) on 20 representative ESEM images for all the investigated samples. For each image, all visible fibers have been measured. More than 350 fibers were measured for each sample. Due to instrumental limitations, the smallest fractions may be overestimated.

The Equivalent Aerodynamic Diameter (D_{ae}) and fiber density of the samples were calculated using the equation by Gonda and Abd El Khalik [66], where d = fiber diameter; β = aspect ratio (fiber length/d); ρ = density; ρ_0 = unit density (1 g/cm). The D_{ae} value is directly related to the deposition region of mineral fiber in the respiratory tract [67]. The formula (molecular weight * number of molecules per unit cell)/(unit cell volume * Avogadro's number) was used to obtain the theoretical density of mordenite samples.

2.3. Thermogravimetric Analysis

Thermogravimetric analysis (TGA) and differential scanning calorimetry (DSC) were performed on the three mordenite samples using a TGA 400 (Perkin Elmer, Waltham, MA, USA) with a heating ramp of 20.0 °C/min under N_2 flow, in a temperature range of 20 to 800 °C.

2.4. Chemical Characterization

Micro-chemical data were collected with a Quanta 400 SEM (FEI, Hillsboro, OR, USA) equipped with an EDX Genesis EDS system following the procedures described in Pacella et al. [68]. Operating conditions were: 15 kV accelerating voltage, 13.4 mm working distance, 0° tilt angle.

For comparison, mordenite crystals embedded in epoxy resin were also analyzed by EMPA using a JXA-8200 WD/ED (Jeol, Akishima, Tokyo, Japan) combined microanalyzer. The quantitative determination of zeolite compositions was performed according to the recommended protocol by Campbell et al. [69], using an acceleration voltage of 15 kV. A series of reference samples, oxides, and silicate minerals with traceable provenience, containing the elements of interest, was measured for calibration. Chemical data reported correspond to the average values calculated from several individual point analyses for each crystal.

The balance error formula E% [70] was used for the selection of the positive analyses. The cut-off was set to ±10%, except for EMPA analyses of SP1 that were considered positive for E% < 12% because of the instability of the sample below the electron beam. The final chemical formulae were calculated after renormalization of the chemical analysis considering the water content determined by thermogravimetric analysis in the case of SEM-EDX, based on 48 (Si+Al) atoms per formula unit (apfu). Owing to the small number of positive analytical points, estimated standard deviations were not reported for EMPA data.

2.5. Inductively Coupled Plasma Atomic Emission Spectrometry (ICP-AES)

ICP-AES was performed on non-purified samples to obtain the composition of eventual impurities and minor elements. The sample dissolution was carried out using the EPA 3052 1996 method. All chemicals used in sample treatment were of Suprapur® grade (Merck KGaA, Darmstadt, Germany); ultrapure water was used for all solutions. For the elemental determination, the EPA 6010D 2018 method was followed, after sample dissolution. Due to the possible impurity of reagents and release from containers and instrumentation, a quality control check was performed. A blank sample was prepared by mixing all reagents and applying the same procedures without adding the samples. Interferences need to be assessed and valid corrections applied, or data need to be flagged to indicate problems. The method's accuracy was verified using recovery tests with a Laboratory Control System (LCS) constituted by a blank sample with known quantities of analytes added to it (reference sample). A difference of 20% in the mean results from the expected values was obtained by replicate preparation and the analysis of the reference sample (analytical standard errors). The reproducibility of metal determinations (precision), based on variation in the analysis of replicates on the same sample, was 10% lower.

2.6. X-ray Powder Diffraction (XRPD)

Fragments of FAS1, GC1, and SP1 were hand-picked under a binocular. The samples were gently ground in an agate mortar and the resulting powders were loaded in 0.7 mm diameter SiO_2-glass capillaries that were aligned on a standard goniometer head. Diffraction patterns were collected on a focusing-beam D8 Advance (Bruker AXS, Karlsruhe, Germany) operating in transmission mode and θ–θ geometry. The instrument is fitted with a PSD VÅntec-1 set to an opening angle of 6° 2θ. Diffraction data were collected in the 5–145° 2θ angular range, 0.022° 2θ step size, and 10 s counting time using CuKα radiation. Rietveld refinements were performed using Topas V.6 [71], which implements the Fundamental Parameters Approach (FPA) [72]. The anisotropic line broadening, caused by the fibrous morphology, was modeled using normalized symmetrized spherical harmonics functions [73]. Absorption effects were corrected by means of the equation of Sabine et al. [74] for a cylindrical sample. Small preferred-orientation effects were accounted by normalized symmetrized spherical harmonics functions, whose appropriate number of terms (sixth-order, nine refinable parameters) was selected following the approach of Ballirano [75].

3. Results

The sample FAS1 is composed of an intergrowth of elongated acicular crystals resulting in soft pink masses of centimetric size. Some large individuals (about 30 μm in width and 280 μm in length) are present from SEM observation (Figure 1a). However, the crystals

show a strong cleavage and fragmentation along the elongation axis, resulting in a chaotic pattern of very small fibers (Figure 1b). The size variability of these fibers is significant, ranging from 0.1 μm to 6 μm in terms of width, and from 4 μm to 80 μm in terms of length. However, the great part of the measured fibers belongs to a small size range. In particular, almost all the fibers (about 96% of the total) have a diameter value lower than 3 μm. The remaining fraction has a width between 3 μm and 5 μm (about 3%) or is bigger than 5 μm (about 1%). Regarding the length values, about 57% of the total of the measured fibers is lower than 20 μm, while the remaining part (about 43%) lies in the range from 20 to 100 μm (Table 1). For regulatory purposes, the most considered sizes of inhalable fibers are: length >5 μm, diameter <3 μm, diameter–length ratio >1:3 [76]. Moreover, according to Stanton's hypothesis [77], fibers with length >8 μm and diameter <0.25 μm are the most able to induce lung disease. For these reasons, accurate measurement of mordenite fibers is of paramount importance.

The sample GC1 is formed by soft woolly masses of centimetric size, with variable colors ranging from pink to brown, but always with a soft appearance. In SEM images, the acicular-to-fibrous crystals show a very elongated habit (Figure 1c). The bigger acicular individuals have a length of about 140 μm and about 20 μm in width, but also in this sample, high cleavage evidence is present (Figure 1d). Similar to the previous samples, also the mordenite fibers from GC1 show a wide size variability, ranging from 0.1 μm to 7 μm in width and from 5 μm to 70 μm in length, but the fibers are distributed in a small range of dimensions. About 92% of the total measured fibers have a width thinner than 3 μm, while the remaining fraction has a bigger size: about 6% lies in the range 3 μm–5 μm, and about 2% is bigger than 5 μm. As regards the length, about 64% of the total is lower than 20 μm, while about 36% lies in the range of 20 μm–100 μm (Table 1).

Similarly, in the sample SP1, very elongated crystals with acicular-to-fibrous habit, strictly intergrow, resulting in pink masses of centimetric size, sometimes with a soft aspect. From SEM image observation, in general, the bigger fragments (about 80 μm in width and 300 μm in length, (Figure 1e) show a strong cleavage and fragmentation and are formed by a great number of smaller needles and fibers (Figure 1f). The mechanical behavior of the fibers is always rigid. Sometimes, also the small fibers show a cleavage pattern parallel to the elongation axis. Accurate measurements of the detected fibers were performed on several SEM images. The results are summarized in Table 1. In particular, the small fibers separated from bigger crystals show wide size variability, ranging from less than 0.1 μm to 8 μm in width and from 4 μm to 170 μm in length. Regarding diameter, 78% of the fibers have a width up to 3 μm, about 6% range between 3 and 5 μm, while for the remainder (about 15%) the diameter is bigger than 5 μm. As regards the length values, 46% of the total of the measured fibers are lower than 20 μm, while about 40% lie in the range from 20 μm to 100 μm. The remaining part (about 13%) of the fibers are longer than 100 μm, up to 170 μm.

The TGA analysis showed a significant weight loss at 450 °C, associated with H_2O loss. The resulting water content of the studied mordenite samples is 14.70 wt% for FAS1, 13.00 wt% for GC1 sample, and 12.70 wt% for SP1 sample.

Microchemical data collected by SEM-EDX and EMPA provided similar oxides concentrations (Table 2), and they scale reasonably well albeit, as expected, differences were observed caused by the onset of the different mechanisms discussed in Pacella et al. [68]. In general, obtaining reliable EMPA data was difficult owing to the morphological and mechanical features of the fibers and only a minor fraction of the analytical points measured were considered positive. This is especially true for sample SP1, whose analyses generally returned high E% values and a total extra-framework site scattering (s.s.) significantly lower than expected from crystal–chemical reasoning and comparison with reference data. For this reason, we will discuss in the following the microchemical data collected by SEM-EDX.
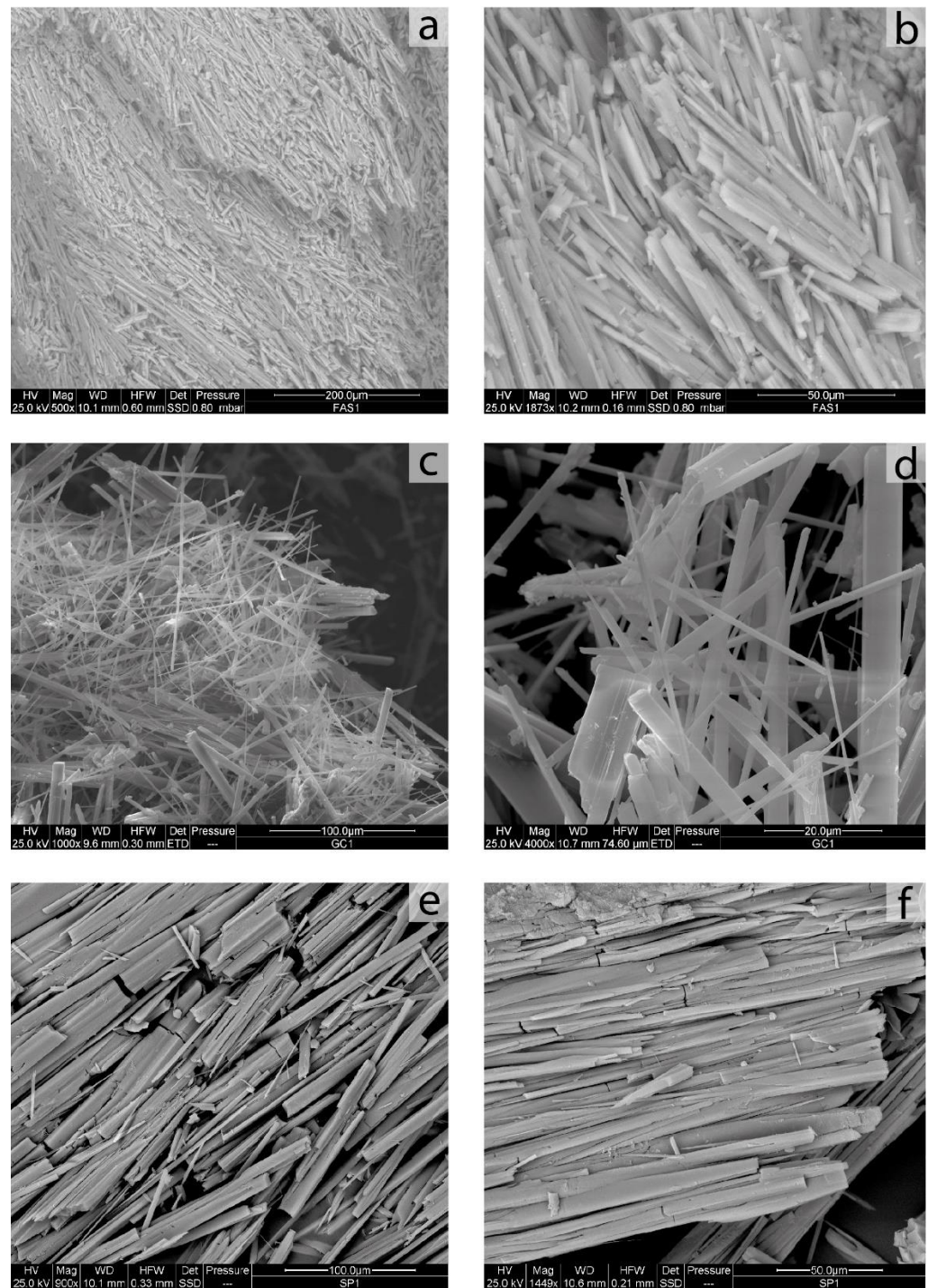
Figure 1. Representative SEM images of the studied samples. (**a**) Masses of elongated crystals of mordenite (FAS1); (**b**) detail of chaotic fragments and small fibers on the surface of the sample (FAS1); (**c**) panoramic image of woolly masses of fibers (GC1) and (**d**) particular of thin fibers and fragments (GC1); (**e**) image of prismatic-to-fibrous crystals of mordenite (SP1); (**f**) detail of small fragments and fibers present on the sample (SP1).

Table 1. Fiber size of investigated mordenites.

WIDTH	FAS1	GC1	SP1
<3 μm	95.56%	92.02%	78%
3–5 μm	3.33%	6.27%	6.50%
>5 μm	1.11%	1.71%	15.50%
min	0.1 μm	0.1 μm	0.1 μm
max	6 μm	7 μm	8 μm
σ	1.04	1.25	2.13
LENGTH			
<20 μm	56.67%	63.82%	46%
20–100 μm	43.33%	36.18%	40.50%
100–200 μm	0	0	13.50%
min	4 μm	5 μm	4 μm
max	80 μm	70 μm	170 μm
σ	14.49	14.50	44.29

Table 2. SEM-EDX and EMPA chemical analyses of the mordenite samples.

Oxides (wt.%)	FAS1		GC1		SP1	
	SEM-EDX	EMPA	SEM-EDX	EMPA	SEM-EDX	EMPA
SiO_2	65.62 (56)	63.32	68.66 (31)	66.55	68.02 (61)	67.43
Al_2O_3	12.46 (26)	11.60	11.79 (51)	10.74	12.23 (25)	10.72
Na_2O	3.41 (50)	2.58	2.85 (37)	1.79	2.34 (45)	1.08
K_2O	0.21 (6)	0.06	0.48 (18)	0.90	1.23 (13)	1.33
MgO	0.19 (14)	-	0.07 (2)	-	0.15 (10)	-
CaO	3.41 (31)	3.94	3.15 (17)	3.49	3.33 (24)	3.54
BaO	-	0.11	-	0.08	-	-
H_2O *		14.70		13.00		12.70
Total	100.00	96.31	100.00	96.55	100.00	96.80
Si	39.22 (21)	39.48	39.92 (12)	40.33	39.61 (15)	40.43
Al	8.78 (21)	8.52	8.08 (12)	7.67	8.39 (15)	7.57
Na	3.95 (50)	3.12	3.21 (38)	2.10	2.64 (53)	1.26
K	0.16 (5)	0.06	0.36 (14)	0.70	0.91 (9)	1.02
Mg	0.17 (11)	-	0.06 (2)	-	0.13 (9)	-
Ca	2.18 (19)	2.64	1.96 (13)	2.27	2.08 (15)	2.27
Ba	-	0.03	-	0.02	-	-
extrafram. cat. s.s. (e^-)	92.2 (116)	89.7	82.1 (96)	82.7	89.5 (117)	78.61
O	96.02 (24)	95.90	95.77 (12)	95.85	95.79 (17)	95.62
H_2O	28.30 (12)	30.57	25.21 (6)	26.27	24.61 (10)	25.39
E%	−0.46	0.28	6.10	4.09	5.30	11.06
R	0.817 (4)	0.822	0.832 (2)	0.840	0.825 (4)	0.842
M/(M+D)	0.636 (44)	0.545	0.638 (32)	0.551	0.617 (36)	0.500

* From TGA data. E% = [Al − (Na + K) + 2 (Mg + Ca + Sr + Ba + Fe^{2+})]/[(Na + K) + 2 (Mg + Ca + Sr + Ba + Fe^{2+})]; R = Si/(Si + Al); M = Na + K; D = Ca + Mg + Mn.

The chemical formulae of the mordenite samples, obtained as an average of reliable SEM-EDX point analysis, are shown in Table 3. The unit formulae were calculated based on 96 oxygens.

Table 3. Chemical formula of the studied mordenite crystals.

Sample	Sampling Area	Chemical Formula
FAS1	Val Duron (TN)	$(Na_{3.95}Ca_{2.18}K_{0.16}Mg_{0.17})[Al_{8.78}Si_{39.22}O_{96}]28.30H_2O$
GC1	Do' Le Pale (TN)	$(Na_{3.21}Ca_{1.96}K_{0.36}Mg_{0.06})[Al_{8.08}Si_{39.92}O_{96}]25.21H_2O$
SP1	Torrebelvicino (VI)	$(Na_{2.64}Ca_{2.08}K_{0.91}Mg_{0.13})[Al_{8.39}Si_{39.61}O_{96}]24.61H_2O$

The three samples have a similar chemical composition and may be identified as Na-rich mordenites. The prevailing extra-framework cations are in the Na > Ca > K relationship. The M/(M+D) ratio (M = Na + K; D = Ca + Mg + Mn) is in the 0.617–0.638 range. K content

becomes relevant in GC1 (0.36 apfu) and especially in SP1 (0.91 apfu). Mg content is very low and consistently <0.2 apfu.

ICP-AES, performed on non-purified samples, indicated the occurrence of low contents of Ba, in the range 578–7400 mg/kg, and Sr in the range 710–3620 mg/kg (Table 4). The occurrence of minor Ba was confirmed by EMPA at some analytical points (max. 0.20 wt% BaO, corresponding to 0.05 apfu Ba in GC1). A significant amount of Fe (range 2070–7500 mg/kg) and Mn (601–27,200 mg/kg) were also detected by ICP-AES (Table 4).

Table 4. Minor elements (mg/kg) of the studied samples from ICP-AES analyses.

Elements	FAS1	GC1	SP1
Ba	1240	7400	578
Sr	710	1210	3620
Fe	7500	6800	2070
Mn	21,900	27,200	601

The value of D_{ae} has been calculated for all the mordenite samples using the equation of Gonda and Abd El Khalik [66]. The 50th percentile of diameter and length were used as the mean value, as suggested by Di Giuseppe [47]. The size parameters, the theoretical density of the mordenite samples and the related D_{ae} values obtained by Gonda's equation [66] are shown in Table 5. For the sample FAS1 the resulting D_{ae} is 2.69 μm, for GC1 is 1.19 μm, while for the sample SP1 is 3.91 μm.

Table 5. Size parameters, theoretical density, and calculated aerodynamic diameter of studied mordenite fibers.

Sample	Mean L (μm)	Mean D (μm)	Theoretical Density (g/cm^3)	D_{ae} (μm)
FAS1	17	1	2.13	2.69
GC1	17	0.4	2.09	1.19
SP1	22	1.5	2.08	3.91

Although mordenite crystallizes in *Cmc*2$_1$, similarly to several crystallographic studies involving the analysis of its structure (e.g., Passaglia et al., Elsen et al., Martucci et al., Lotti et al. [12,78–80]) we refined the various samples in the centrosymmetric *Cmcm* space group. This is justified by the relevant pseudo-centrosymmetry of the mordenite structure and by the corresponding significant reduction in the number of refined parameters.

Starting structural parameters were taken from Mortier et al. [81] for a rehydrated Ca-exchanged mordenite owing to chemical similarities. The model includes two partly occupied cation sites (Ca1 and Ca2) located, respectively, at the center of the strongly compressed eight-member channel (8MRc) and within the ellipsoidal twelve-membered ring (12MRc) channel. H$_2$O molecules populate five sites (OW1 within 8MRc; OW3, OW4 and OW5 within 12MRc; OW2 within the side-pocket parallel to (010)), in some cases partly occupied and possibly affected by H$_2$O/cation disorder.

Preliminary analysis of the various patterns revealed the occurrence of quartz (FAS1: abundant; GC1 and SC1: minor) and a 15 Å phyllosilicate phase (FAS1: minor). In the initial stages of the refinements, isotropic displacement parameters of mordenite were refined for groups of atoms (all tetrahedral cations, all framework oxygens, all extra-framework cations), keeping fixed those of the oxygen atoms of H$_2$O to the average value calculated from the structural data of Simoncic and Armbruster [5]. In the final cycle of refinement, individual isotropic displacement parameters of the framework atoms were refined. Moreover, s.s. at extra-framework cation and H$_2$O sites were refined. Neutral scattering curves of Si, O, and Ca were used for modeling the framework and the extra-framework cation sites. The population of Al vs. Si at the various tetrahedral sites T was iteratively adjusted to conform to the calculated population from the analysis of

the corresponding <T–O> using the Jones's equation [82]. Fully ionized O-2 scattering curves were used for modelling the H_2O molecule sites to empirically compensate for the presence of the bonded hydrogen atoms. Using this approach, the total H_2O pfu was refined to a value close to that expected from crystal–chemical reasoning and TGA data. Starting structural data of quartz were those of Le Page and Donnay [83]. The full structure refinement of quartz was performed in the case of sample FAS1, whereas, in the remaining samples, only the scale factor was optimized along with a single parameter for modeling the crystallite dependence of the peak broadening.

Miscellaneous data of the refinements are reported in Table 6, and relevant structural data in Table 7. Rietveld plots of sample SP1 are shown, as an example, in Figure 2. CIFs were deposited as Supplementary Materials and are available for download at the journal's site.

Table 6. Miscellaneous data of the refinements. Statistic indicators as defined in Young [84]. Data of Mortier et al. [81] are reported for comparison (M76).

	FAS1	GC1	SP1	M76
Rwp	0.029	0.027	0.043	-
Rp	0.022	0.078	0.031	-
DWd	0.354	0.530	0.479	-
χ^2	3.943	3.664	4.535	-
R_{Bragg}	0.009	0.011	0.019	-
quartz wt%	44.14 (14)	4.44 (5)	3.35 (4)	-
a (Å)	18.1191 (2)	18.1097 (3)	18.11029 (18)	18.122 (8)
b (Å)	20.4598 (2)	20.4488 (2)	20.46837 (17)	20.457 (10)
c (Å)	7.52370 (7)	7.51783 (7)	7.52054 (6)	7.515 (4)
V (Å^3)	2789.13 (5)	2783.64 (6)	2787.77 (4)	2786.0 (10)

Table 7. Average isotropic displacement parameters (B_{iso}) and extra-framework cation and H_2O molecule site population. Isotropic displacement parameters of H_2O molecule sites were kept fixed throughout the refinements. Data of Mortier et al. [81] are reported for comparison (M76). Letters between parentheses refer to the notation of extra-framework sites used by Martucci et al. [79], modified from Mortier [85].

	FAS1	GC1	SP1	M76
$B_{T1,4}$ * (Å^2)	1.55	1.68	1.73	1.432
$B_{O1,10}$ * (Å^2)	2.59	3.21	2.93	3.45
$B_{Ca1,2}$ * (Å^2)	4.3 (3)	3.6 (2)	4.72 (19)	3.99
$B_{OW1,5}$ * (Å^2)	10.92	10.92	10.92	12.75
occ. Ca1 (A)	0.610 (7)	0.584 (6)	0.575 (6)	0.425 (8)
occ. Ca2 (F)	0.384 (8)	0.385 (8)	0.385 (6)	0.420 (8)
extrafram. cat. s.s. (e$^-$)	79.5 (12)	77.5 (11)	76.8 (10)	67.6 (13)
extrafram. cat. s.s. (e$^-$) from chemical data	92.2	82.1	89.5	66.6
occ. OW1 (B)	1.085 (16)	1.086 (13)	1.050 (12)	0.99 (2)
occ. OW2 (C)	0.544 (8)	0.462 (6)	0.465 (5)	1.18 (5) **
occ. OW3 (D)	1.061 (14)	0.880 (14)	0.967 (11)	0.85 (3)
occ. OW4 (J)	0.679 (6)	0.604 (5)	0.634 (5)	0.644 (13)
occ. OW5 (E)	0.983 (9)	1.018 (9)	0.937 (7)	1.088 (13)
H_2O pfu	31.7 (4)	29.4 (3)	29.4 (3)	31.1 (7)
H_2O pfu from TGA	28.30	25.21	24.61	-

* Average value. Ca1 and Ca2 displacement parameters were constrained to be equal. OW displacement parameters were kept fixed to the listed value. Individual B_{iso} may be found in the Supplementary Files. ** Value that refers to a site having halved multiplicity as compared to that of the present samples (see text for explanation).
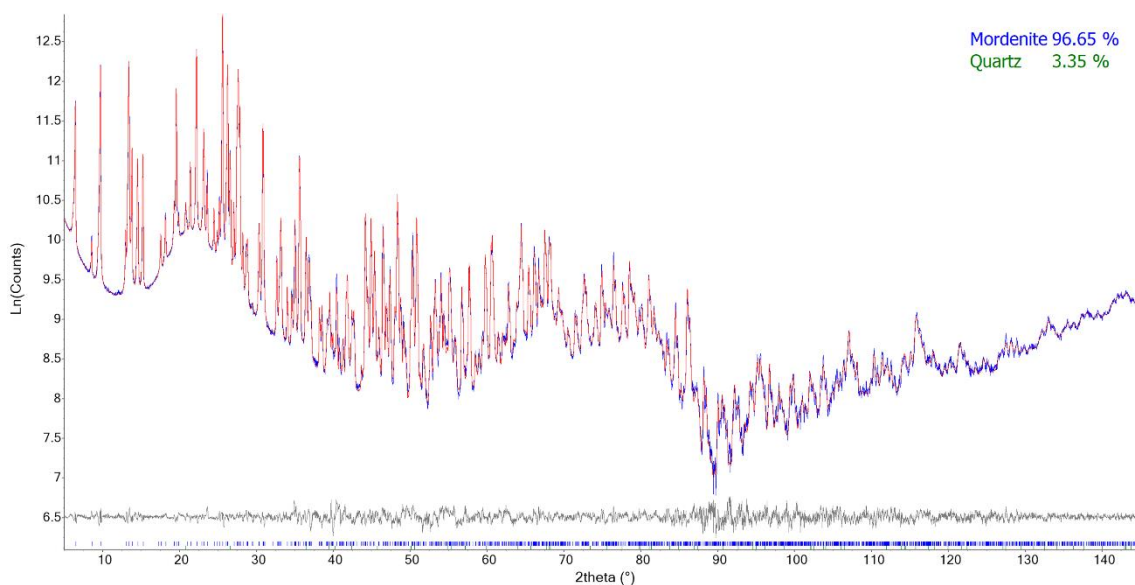
Figure 2. Conventional Rietveld plots of sample SP1. Intensity reported in logarithmic (natural) scale. Blue continuous line: experimental; red continuous line: calculated; grey continuous line: difference; below: vertical ticks color codes of Bragg reflections: blue mordenite; green quartz.

4. Discussion

Mordenite crystals from the three investigated samples are characterized by similar structural features (Figure 3). The <T–O> bond distances refined in the 1.602–1.647 Å range pointing out to some Si,Al ordering. Individual T–O bond distances are slightly spread as compared to refinements carried out in *Cmc*2$_1$ [5,8]. This behavior is coherent with the absence of restraints on bond distances and is marginally more pronounced for FAS1 owing to the presence in mixture of a relevant amount of quartz (Table 6). The unit cell volumes are in the following relationship: FAS1 > SP1 > GC1 (Table 6), and this behavior correlates with both the decreasing Al content determined from SEM-EDX and that estimated from the Jones's equation [82] (Table 2). It has been shown that this equation, as well as other more accurate calculation procedures [86,87], underestimates the Al content of mordenite samples [5]. This underestimation has been attributed to the shortening of T–O bond distances caused by the apparent symmetry being higher than the true one [87]. For example, the calculated R = Si/(Si+Al) of the sample of Ca-exchanged mordenite analyzed by Mortier et al. [81] is 0.912 as compared to 0.846 from chemical data. Present data confirm such behavior as R was calculated in the 0.895–0.914 range, which is higher than 0.817–0.832 from SEM-EDX analyses. The latter range is coherent with the chemical analyses of natural mordenite samples (R = 0.80–0.86 [3]). Al consistently exhibits the following site-specific occupation preference: T3 > T4 > T1 > T2 sequence (Table 8) in close agreement with reference data [5,81,87], confirming its prevailing allocation at T3 and, subordinately, at T4, i.e., the tetrahedra build the four-membered ring. The retrieved mutual extra-framework cations/H_2O molecule distribution is clearly affected by the simplification used to refine the structure in the *Cmcm* space group. This approximation does not permit a detailed discussion of those structural details and for this reason, only a few features will be underlined. Both position and s.s. of the extra-framework cation and H_2O sites are close to those of Mortier et al. [81], except for OW2, which was allowed to move freely from the center of the pocket in correspondence of the extra-framework site C of Mortier [85], and as a result, it was found to be slightly off-axis. The total extra-framework cation s.s. of the three samples is rather constant, being in the 76.8(10)–79.5(14) e$^-$ range and is smaller than that determined from SEM-EDX (82.1–92.2). The Ca1 site is eight-fold coordinated to six oxygen atoms of the framework (4 × O1; 2 × O9) and to two H_2O molecules lying at OW1, which is consistently fully occupied. Ca2 is at bonding distance exclusively with H_2O molecules (OW3, OW4, and OW5). OW3 and OW5 are almost fully occupied, whereas OW4

is approximately half-occupied in agreement with the mutually excluding short OW4–OW4 contacts. This leads to a seven-fold coordination for Ca2. The H_2O content is also constant, being in the 29.4(3)–31.7(4) molecule pfu range, in reasonable agreement with both present and reference chemical data [3]. It is worth noting that OW2 is at bonding distances with other H_2O molecule sites allocated in the neighboring channels (OW1 in 8MRc and OW3 in 12MRc, respectively). TGA points to a higher H_2O content of FAS1 with respect to GC1 and SP1 coherently with the refined s.s. (Table 7). The total number of H_2O molecules pfu derived from the structure refinements is regularly higher than that determined by TGA, suggesting the occurrence of some H_2O/cation disorder. This hypothesis is supported by the total extra-framework cation s.s. of the three samples from Rietveld refinement being smaller than that retrieved from SEM-EDX.
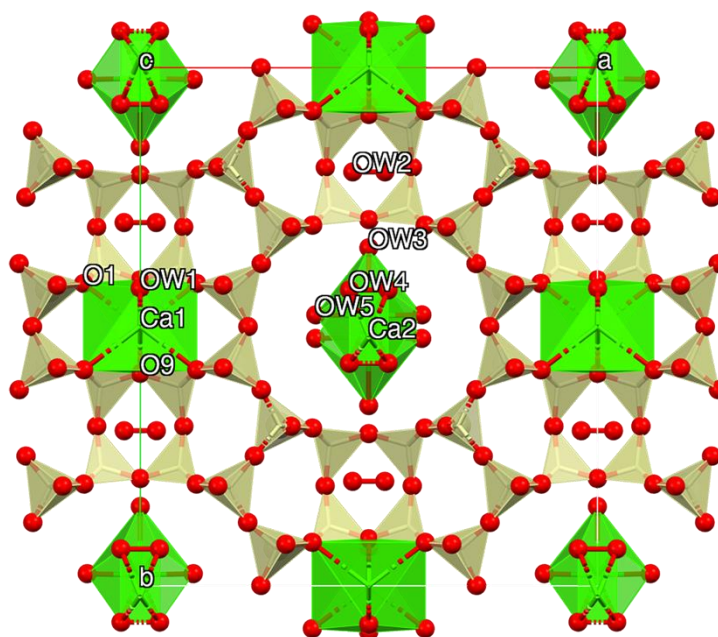
Figure 3. Sketch of the refined structure of SP1 as seen along [001].

As previously described, the three samples show comparable chemical compositions, and the only differences regard extra-framework cations, water content, and the amount of impurities. Despite the crystal habit being always fibrous, significant differences in the fiber's size were observed in the studied samples. The obtained D_{ae} values are 2.69 μm for the sample FAS1, 3.91 μm for SP1, and 1.19 μm for GC1. Considering that particles with D_{ae} value up to 10 μm can pass the larynx (thoracic fraction) and particles with $D_{ae} < 4$ μm are able to reach the alveolar region (respirable fraction) [88], in all the studied samples a fraction of fibers are respirable and could enter into the alveolus. However, the variability of the D_{ae} value highlights the possibility that the hazard of mordenite fibers to humans could be significantly different, depending on the sample features, and needs to be evaluated case by case. Considering the similar structural and chemical features compared to other carcinogenic zeolites (e.g., erionite), fibrous mordenite should be considered potentially hazardous for humans.

In acid conditions (e.g., cellular environment—macrophages) the Si/Al framework ratio is fundamental to guide the dissolution rate. Zeolites with a high Si/Al ratio show a slower dissolution, resultantly being more biodurable [51,89]. In particular, zeolite dissolution can result in (I) stoichiometric framework degradation and silicate precipitation (Si/Al = 1); (II) partially dissolved silicate framework with selective removal of aluminum and then partially dissolved silicate particles (Si/Al = 2); (III) intact silicate framework (Si/Al = 3). In the last case, the aluminum is insufficient to weaken the structure and cause silicon dissolution. Thus, little or no precipitation is observed, and amorphous

undissolvable silicate particles remain intact [89]. For this reason, it is important to consider the higher Si/Al ratio of the studied mordenite samples (4.47 for FAS1, 4.94 for GC1, and 4.72 for SP1) compared to erionite (about 3.5) [47].

Table 8. Relevant bond distances (Å). The Al population at the various tetrahedral sites T (% Al) and the corresponding R = Si/(Si+Al) were calculated using the equation of Jones [82]. Data of Mortier et al. [81] are reported for comparison (M76). Due to short OW4–OW4 contacts, only half of the Ca2–OW4 distances are effectively occurring.

	FAS1	GC1	SP1	M76
T1–O3	1.598 (7)	1.595 (7)	1.590 (5)	1.600 (4)
T1–O1	1.599 (6)	1.620 (7)	1.621 (5)	1.617 (4)
T1–O7	1.661 (5)	1.620 (4)	1.639 (3)	1.625 (5)
T1–O6	1.641 (4)	1.654 (3)	1.631 (2)	1.617 (4)
<T1–O>	1.625	1.622	1.620	1.615
% Al at T1	13.5	11.9	10.6	7.1
T2–O8	1.582 (3)	1.591 (3)	1.596 (3)	1.584 (4)
T2–O5	1.621 (3)	1.608 (3)	1.605 (2)	1.620 (4)
T2–O2	1.584 (6)	1.604 (6)	1.611 (4)	1.609 (4)
T2–O3	1.622 (8)	1.617 (8)	1.603 (6)	1.600 (4)
<T2–O>	1.602	1.605	1.604	1.603
% Al at T2	0	0.9	0.1	0
T3–O4	1.604 (12)	1.571 (11)	1.593 (9)	1.598 (4)
T3–O9	1.638 (6)	1.646 (6)	1.656 (5)	1.646 (4)
T3–O1 × 2	1.673 (7)	1.657 (6)	1.663 (5)	1.639 (4)
<T3–O>	1.647	1.633	1.644	1.631
% Al at T3	27.8	18.7	25.7	17.2
T4–O2 × 2	1.620 (7)	1.595 (5)	1.616 (4)	1.622 (4)
T4–O4	1.614 (12)	1.649 (11)	1.631 (9)	1.614 (4)
T4–O10	1.612 (6)	1.623 (5)	1.616 (4)	1.624 (4)
<T4–O>	1.617	1.616	1.620	1.621
% Al at T4	8.2	7.6	10.3	10.8
<T–O>	1.623	1.619	1.622	1.619
Al_{cal} pfu	5.05	4.15	4.59	4.23
Al pfu from chemical data	8.78	8.08	8.39	7.4
R_{cal} = Si/(Si+Al)	0.895	0.914	0.904	0.912
R from chemical data	0.817	0.832	0.825	0.846
Ca1–OW1 × 2	2.402 (11)	2.393 (8)	2.413 (8)	2.292 (6)
Ca1–O9 × 2	2.644 (10)	2.679 (9)	2.634 (7)	2.688 (6)
Ca1–O1 × 4	2.867 (6)	2.861 (6)	2.856 (4)	2.878 (4)
<^{VIII}Ca1–O>	2.695	2.699	2.690	2.684
Ca2–OW5 × 2	2.076 (12)	2.024 (12)	2.104 (10)	2.270 (7)
Ca2–OW4 × 4 (× 2)	2.611 (11)	2.493 (9)	2.527 (8)	2.459 (7)
Ca2–OW4 × 4 (× 2)	2.532 (14)	2.546 (11)	2.563 (10)	2.475 (7)
Ca2–OW3	2.90 (2)	2.690 (17)	2.704 (16)	2.524 (10)
<^{VII}Ca2–O>	2.466	2.399	2.427	2.380

Moreover, as observed by EMPA and ICP-AES, low but significant contents of Fe, Mn, Ba, and Sr were detected on natural samples. The role of some elements detected on the fibers or in attached impurities (including minor and trace elements), such as Fe, Mn, As, Pb, Cr, Ni, Po, and others, is very important for the toxicity of fibrous minerals as demonstrated by the wide literature [51,61,65,90]. Therefore, the oxidation state and the amount of iron or other cations on mordenite fibers could play an important role in its toxicity, as observed for asbestos and other zeolites. In fact, the presence of iron nanoparticles is considered as one of the key factors for explaining fiber toxicity. Iron exposed at the fiber surface, especially Fe^{2+}, is considered to play a primary role for Reactive Oxygen Species (ROS) production [90]. Moreover, Mn resulted in being cytotoxic to human lung cells (in vitro) at concentration ranges of 0.2–200 μM [91].

Considering the important amount of mordenite fiber and mass in the volcanic rocks of the sampling areas, and the resulting features of these fibers, attention could be focused on managing this mineral and hosting rocks, especially in case of active mining or quarrying activities and in the use of such material. However, further detailed studies are needed. As known, the evaluation of the toxicity and carcinogenicity of mineral fibers is a complex task. Still, at the same time, it is fundamental to plan activities and safety rules, especially regarding occupationally exposed subjects. Our work represents a further step through the knowledge of morphometric, physical, and chemical characteristics of mordenite. As a matter of fact, together with bio-durability, surface activity, and correlation with human epidemiological observations, these parameters play a crucial role in evaluation of toxicity and carcinogenicity of mineral fibers [92,93].

5. Conclusions

At present, fibrous mordenite is considered a non-carcinogenic mineral for humans and is classified as Group 3 by IARC [44]. However, this classification is essentially due to the lack of detailed data on this zeolite. Despite the abundance of natural mordenite in many worldwide zeolitized volcanic rocks, and the number of industrial applications of this mineral, few studies have investigated the chemical, structural, physical, and toxicological character of mordenite fibers. In the present work, three different samples of fibrous mordenite from Northern Italy were investigated in detail, with the aim of defining their size parameters, the crystal structure, and the chemical composition of mordenite and detected impurities.

The calculated D_{ae} values are 1.19 μm for the GC1 sample, 2.69 μm for FAS1, and 3.91 μm for SP1, meaning that all the studied samples could spread fibers which can be considered "respirable" for humans. From the chemical point of view, all the mordenite samples are Na-rich (Na > Ca > K). The presence of Ba, Sr, Fe, and Mn was also detected in non-purified samples, and these elements could play a crucial role in the toxicity of mordenite fibers. The structural features of the investigated samples are similar, and the unit cell volume follows the series FAS1 > SP1 > GC1, reflecting Al content decreasing. The higher Si/Al ratio of mordenite (about 4.7) compared to erionite (about 3.5) could also play an important part in its biodurability.

These results contribute to increasing the knowledge of this important fibrous zeolite, especially from the mineralogical (crystal structure and chemistry) and physical (morphology and size parameters) points of view, and are the basis for a further study on the toxicological implications of this zeolite. In any case, the data obtained in this work indicate that fibrous mordenite may represent a potential health hazard and should be tested for toxicity and carcinogenicity, as it could be a non-safe zeolite.

Author Contributions: M.G.: Conceptualization, Supervision, Investigation, Data curation, Writing—original draft, writing—review and editing. P.B. and A.P.: Formal analysis, Investigation, Data curation, Writing—review and editing. M.A.M., C.R. and F.D.L.: Data curation, Writing—review and editing. I.F.: Formal Analysis. M.M.: Conceptualization, Data Curation, Writing—review and editing, Funding Acquisition. All authors have read and agreed to the published version of the manuscript.

Conflicts of Interest: The authors declare no conflict of interest. The funders had no role in the design of the study; in the collection, analyses, or interpretation of data; in the writing of the manuscript, or in the decision to publish the results.

References

1.　How, H. On mordenite, a new mineral from the trap of Nova Scotia. *J. Chem. Soc.* **1864**, *17*, 100–104.

2.　Passaglia, E. The Crystal Chemistry of Mordenites. *Contrib. Mineral. Petrol.* **1975**, *50*, 65–77. [CrossRef]

3.　Passaglia, E.; Sheppard, R.A. The crystal chemistry of zeolites. In *Natural Zeolites: Occurrence, Properties Application*; Bish, D.L., Ming, D.W., Eds.; Mineralogical Society of America and Geochemical Society: Washington, DC, USA, 2001; pp. 69–116.

4.　Baerlocher, C.; McCusker, L.B.; Olson, D.H. *Atlas of Zeolite Framework Types*, 6th ed.; Elsevier: Amsterdam, The Netherlands, 2007.

5.　Simoncic, P.; Armbruster, T. Peculiarity and defect structure of the natural and synthetic zeolite mordenite: A single-crystal X-ray study. *Am. Mineral.* **2004**, *89*, 421–431. [CrossRef]

6.　Armbruster, T.; Gunter, M.E. Crystal structures of natural zeolites. In *Natural Zeolites: Occurrence, Properties, Applications*; Bish, D.L., Ming, D.W., Eds.; Reviews in Mineralogy and Geochemistry; Mineralogical Society of America and Geochemical Society: Washington, DC, USA, 2001; Volume 45, pp. 1–68.

7.　Meier, W.M. The crystal structure of mordenite (ptilolite). *Z. Für Krist.* **1961**, *115*, 439–450. [CrossRef]

8.　Alberti, A.; Davoli, P.; Vezzalini, G. The crystal structure refinement of a natural mordenite. *Z. Für Krist.-Cryst. Mater.* **1986**, *175*, 249–256. [CrossRef]

9.　Zhang, L.; Xie, S.; Xin, W.; Li, X.; Liu, S.; Xu, L. Crystallization and morphology of mordenite zeolite influenced by various parameters in organic-free synthesis. *Mater. Res. Bull.* **2011**, *46*, 894–900. [CrossRef]

10.　Pongiluppi, D. Ulteriori notizie sulle zeoliti della Sardegna. *Rend. Soc. Ital. Miner. Petrol.* **1974**, *30*, 1201–1205.

11.　Mormone, A.; Piochi, M. Mineralogy, geochemistry and genesis of zeolites in Cenozoic pyroclastic flows from the Asuni area (Central Sardinia, Italy). *Minerals* **2020**, *10*, 268. [CrossRef]

12.　Passaglia, E.; Artioli, G.; Gualtieri, A.; Carnevali, R. Diagenetic mordenite from Ponza, Italy. *Eur. J. Mineral.* **1995**, *7*, 429–438. [CrossRef]

13.　Brigatti, M.F.; Gottardi, G. Le zeoliti nelle porfiriti dell'Alta Valle del Cordevole (Belluno). *Per. Mineral.* **1971**, *40*, 27.

14.　Vezzalini, G.; Alberti, A. Le zeoliti dell'Alpe di Siusi. *Rend. Soc. Ital. Miner. Petrol.* **1975**, *31*, 711–719.

15.　De Vecchi, G.P.; Sedea, R. The Paleogene basalt of the Veneto region (NE Italy). *Mem. Inst. Geol. Mineral. Univ. Padua* **1995**, *47*, 253–274.

16.　Galli, E. La phillipsite barifera ("wellsite") di M. Calvarina (Verona). *Period. Di Mineral.* **1972**, *41*, 23–33.

17.　Passaglia, E.; Tagliavini, A.; Gutoni, R. Offretite and other zeolites from Fittà (Verona, Italy). *Neues Jahrb. Für Mineral. Mon.* **1996**, *9*, 418–428.

18.　Mattioli, M.; Cenni, M.; Passaglia, E. Secondary mineral assemblages as indicators of multi stage alteration processes in basaltic lava flows: Evidence from the Lessini Mountains, Veneto Volcanic Province, Northern Italy. *Per. Mineral.* **2016**, *85*, 1–24.

19.　Mattioli, M.; Cenni, M. First Occurrence of Willhendersonite in the Lessini Mounts, Northern Italy. *Crystals* **2021**, *11*, 109. [CrossRef]

20.　Giordani, M.; Mattioli, M.; Dogan, M.; Dogan, A.U. Potential carcinogenic erionite from Lessini Mounts, NE Italy: Morphological, mineralogical and chemical characterization. *J. Toxicol. Environ. Health A* **2016**, *79*, 808–824. [CrossRef]

21.　Giordani, M.; Mattioli, M.; Ballirano, P.; Pacella, P.; Cenni, M.; Boscardin, M.; Valentini, L. Geological occurrence, mineralogical characterization and risk assessment of potentially carcinogenic erionite in Italy. *J. Toxicol. Environ. Health B* **2017**, *20*, 81–103. [CrossRef]

22.　Cangiotti, M.; Battistelli, M.; Salucci, S.; Falcieri, E.; Mattioli, M.; Giordani, M.; Ottaviani, M.F. Electron paramagnetic resonance and transmission electron microscopy study of the interactions between asbestiform zeolite fibers and model membranes. *J. Toxicol. Environ. Health A* **2017**, *80*, 171–187. [CrossRef]

23.　Mattioli, M.; Giordani, M.; Arcangeli, P.; Valentini, L.; Boscardin, M.; Pacella, A.; Ballirano, P. Prismatic to Asbestiform Offretite from Northern Italy: Occurrence, Morphology and Crystal-Chemistry of a New Potentially Hazardous Zeolite. *Minerals* **2018**, *8*, 69. [CrossRef]

24.　Mattioli, M.; Ballirano, P.; Pacella, A.; Cangiotti, M.; Di Lorenzo, F.; Valentini, L.; Meli, M.A.; Roselli, C.; Fagiolino, I.; Giordani, M. Fibrous ferrierite from Northern Italy: Mineralogical, chemical, and EPR characterization and assessment of potential toxicity. *Minerals* 2022, *in press*.

25.　Castellarin, A.; Lucchini, F.; Rossi, P.L.; Selli, L.; Simboli, G. The Middle Triassic magmatic-tectonic arc development in the Southern Alps. *Tectonophysics* **1988**, *146*, 79–89. [CrossRef]

26. De Zanche, V.; Gianolla, P.; Mietto, P.; Siorpaes, C.; Vail, P.R. Triassic sequence stratigraphy in the Dolomites. *Mem. Di Sci. Geol.* **1993**, *45*, 1e27.
27. Braccio, A. I minerali della Val di Fassa. Dove si trovano e come si presentano. *Natura* **1968**, *42*, 3–48.
28. Davis, M.E. Zeolites and molecular sieves: Not just ordinary catalysts. *Ind. Eng. Chem. Res.* **1991**, *30*, 1675–1683. [CrossRef]
29. Akimkhan, A.M. Structural and ion-exchange properties of natural zeolite. *Ion Exch. Technol.* **2012**, 261–282. [CrossRef]
30. Datt, A. Applications of Mesoporous Silica and Zeolites for Drug Delivery. Ph.D. Dissertation, The University of Iowa, Iowa City, IA, USA, 2012.
31. Zhou, L.; Boyd, C.E. Total ammonia nitrogen removal from aqueous solutions by the natural zeolite, mordenite: A laboratory test and experimental study. *Aquaculture* **2014**, *432*, 252–257. [CrossRef]
32. Kalvachev, Y.; Todorova, T.; Popov, C. Recent Progress in Synthesis and Application of Nanosized and Hierarchical Mordenite—A Short Review. *Catalysts* **2021**, *11*, 308. [CrossRef]
33. Corma, A.; Miguel, P.J.; Orchilles, A.V.; Koermer, G. Zeolite effects on the cracking of long chain alkyl aromatics. *J. Catal.* **1994**, *145*, 181–186. [CrossRef]
34. Gilbert, J.E.; Mosset, A. Large crystals of mordenite and MFI zeolites. *Mater. Res. Bull.* **1998**, *33*, 997–1003. [CrossRef]
35. Lin, J.S.; Wang, J.J.; Wang, J.; Wang, I.; Balasamy, R.J.; Aitani, A.; Al-Khattaf, S.; Tsai, T.C. Catalysis of alkaline-modified mordenite for benzene alkylation of diolefin-containing dodecene for linear alkylbenzene synthesis. *J. Catal.* **2013**, *300*, 81–90. [CrossRef]
36. Wahono, S.K.; Stalin, J.; Addai-Mensah, J.; Skinner, W.; Vinu, A.; Vasilev, K. Physico-chemical modification of natural mordenite-clinoptilolite zeolites and their enhanced CO_2 adsorption capacity. *Microporous Mesoporous Mater.* **2020**, *294*, 109871. [CrossRef]
37. Suzuki, Y. Carcinogenic and fibrogenic effects of zeolites: Preliminary observations. *Environ. Res.* **1982**, *27*, 433–445. [CrossRef]
38. Suzuki, Y.; Kohyama, N. Malignant mesothelioma induced by asbestos and zeolite in the mouse peritoneal cavity. *Environ. Res.* **1984**, *35*, 277–292. [CrossRef]
39. Suzuki, Y.; Kohyama, N. Carcinogenic and fibrogenic effects of erionite, mordenite, and synthetic zeolite 4A. In *Occurrence, Properties and Utilization of Natural Zeolites*; Kallo, D., Sherry, H.S., Eds.; Akadémiai Kiadò: Budapest, Hungary, 1988; pp. 829–840.
40. Tátrai, E.; Bácsy, E.; Kárpáti, J.; Ungváry, G. On the examination of the pulmonary toxicity of mordenite in rats. *Pol. J. Occup. Med. Environ. Health* **1992**, *5*, 237–243. [PubMed]
41. Adamis, Z.; Tátrai, E.; Honma, K.; Six, É.; Ungváry, G. In Vitro and in Vivo Tests for Determination of the Pathogenicity of Quartz, Diatomaceous Earth, Mordenite and Clinoptilolite. *Ann. Occup. Hyg.* **2000**, *44*, 67–74. [CrossRef]
42. Palekar, L.D.; Most, B.M.; Coffin, D.L. Significance of mass and number of fibers in the correlation of V79 citotoxicity with tumorigenic potential of mineral fiber. *Environ. Res.* **1988**, *46*, 142–152. [CrossRef]
43. Fach, E.; Kristovich, R.; Long, J.F.; Waldman, W.J.; Dutta, P.K.; Williams, M.V. The effect of iron on the biological activities of erionite and mordenite. *Environ. Int.* **2003**, *29*, 451–458. [CrossRef]
44. International Agency for Research on Cancer. IARC Working Group on the Evaluation of Carcinogenic Risks to Humans: Silica, Some Silicates, Coal Dust and Para-Aramid Fibrils. 1997. Available online: http://monographs.iarc.fr/ENG/Monographs/vol68/mono68 (accessed on 24 March 2022).
45. Guthrie, G.D. Biological effects of inhaled minerals. *Am. Mineral.* **1992**, *77*, 225–243.
46. Stephenson, D.J.; Fairchild, C.I.; Buchan, R.M.; Dakins, M.E. A fiber characterization of the natural zeolite, mordenite: A potential inhalation health hazard. *Aerosol Sci. Technol.* **1999**, *30*, 467–476. [CrossRef]
47. Di Giuseppe, D. Characterization of fibrous mordenite: A first step for the evaluation of its potential toxicity. *Crystals* **2020**, *10*, 769. [CrossRef]
48. Mattioli, M.; Giordani, M.; Dogan, M.; Cangiotti, M.; Avella, G.; Giorgi, R.; Dogan, A.U.; Ottaviani, M.F. Morpho-chemical characterization and surface properties of carcinogenic zeolite fibers. *J. Hazard. Mater.* **2016**, *306*, 140–148. [CrossRef] [PubMed]
49. Ballirano, P.; Pacella, A.; Bloise, A.; Giordani, M.; Mattioli, M. Thermal Stability of Woolly Erionite-K and Considerations about the Heat-Induced Behaviour of the Erionite Group. *Minerals* **2018**, *8*, 28. [CrossRef]
50. Beaucham, C.; King, B.; Feldmann, K.; Harper, M.; Dozier, A. Assessing occupational erionite and respirable crystalline silica exposure among outdoor workers in Wyoming, South Dakota, and Montana. *J. Occup. Environ. hyg.* **2018**, *15*, 455–465. [CrossRef] [PubMed]
51. Giordani, M.; Cametti, G.; Di Lorenzo, F.; Churakov, S.V. Real-time observation of fibrous zeolites reactivity in contact with simulated lung fluids (SLFs) obtained by atomic force microscope (AFM). *Minerals* **2019**, *9*, 83. [CrossRef]
52. Gualtieri, A.F.; Gandolfi, N.B.; Passaglia, E.; Pollastri, S.; Mattioli, M.; Giordani, M.; Ottaviani, M.F.; Cangiotti, M.; Bloise, A.; Barca, D.; et al. Is fibrous ferrierite a potential health hazard? Characterization and comparison with fibrous erionite. *Am. Mineral. J. Earth Planet. Mater.* **2018**, *103*, 1044–1055. [CrossRef]
53. Zoboli, A.; Di Giuseppe, D.; Baraldi, C.; Gamberini, M.C.; Malferrari, D.; Urso, G.; Lassinantti Gualtieri, M.; Bailey, M.; Gualtieri, A.F. Characterisation of fibrous ferrierite in the rhyolitic tuffs at Lovelock, Nevada, USA. *Mineral. Mag.* **2019**, *83*, 577–586. [CrossRef]
54. Giordani, M.; Mattioli, M.; Cangiotti, M.; Fattori, A.; Ottaviani, M.F.; Betti, M.; Ballirano, P.; Pacella, A.; Di Giuseppe, D.; Scognamiglio, V.; et al. Characterisation of potentially toxic natural fibrous zeolites by means of electron paramagnetic resonance spectroscopy and morphological-mineralogical studies. *Chemosphere* **2022**, *291*, 133067. [CrossRef]
55. Hochella, M.F. Surface chemistry, structure, and reactivity of hazardous mineral dust. In *Health Effects of Mineral Dusts*; Guthrie, G.D., Mossman, B.T., Eds.; Reviews Mineral; Bookcrafters: Chelsea, MI, USA, 1993; Volume 28, pp. 275–308. [CrossRef]

56. Hesterberg, T.W.; Chase, G.; Axten, C.; Miller, W.C.; Musselman, R.P.; Kamstrup, O.; Hadley, J.; Morscheidt, C.; Bernstein, D.M.; Thevenaz, P. Biopersistence of synthetic vitreous fibers and amosite asbestos in the rat lung following inhalation. *Toxicol. Appl. Pharmacol.* **1998**, *151*, 262–275. [CrossRef]

57. Fubini, B. The physical and chemical properties of asbestos fibres which contribute to biological activity. In Proceedings of the Asbestos Health Effect Conference, Oakland, CA, USA, 24–25 May 2001; US Environmental Protection Agency: Washington, DC, USA, 2001.

58. Maxim, L.D.; Hadley, J.G.; Potter, R.M.; Niebo, R. The role of fiber durability/biopersistence of silica-based synthetic vitreous fibers and their influence on toxicology. *Regul. Toxicol. Pharmacol.* **2006**, *46*, 42–62. [CrossRef]

59. Pollastri, S.; Gualtieri, A.F.; Gualtieri, M.L.; Hanuskova, M.; Cavallo, A.; Gaudino, G. The zeta potential of mineral fibres. *J. Hazard. Mater.* **2014**, *276*, 469–479. [CrossRef] [PubMed]

60. Ballirano, P.; Pacella, A.; Cremisini, C.; Nardi, E.; Fantauzzi, M.; Atzei, D.; Rossi, A.; Cametti, G. Fe (II) segregation at a specific crystallographic site of fibrous erionite: A first step toward the understanding of the mechanisms inducing its carcinogenicity. *Microporous Mesoporous Mater.* **2015**, *211*, 49–63. [CrossRef]

61. Bloise, A.; Barca, D.; Gualtieri, A.F.; Pollastri, S.; Belluso, E. Trace elements in hazardous mineral fibres. *Environ. Pollut.* **2016**, *216*, 314–323. [CrossRef] [PubMed]

62. Crovella, S.; Bianco, A.M.; Vuch, J.; Zupin, L.; Moura, R.R.; Trevisan, E.; Schneider, M.; Brollo, A.; Nicastro, E.M.; Cosenzi, A.; et al. Iron signature in asbestos-induced malignant pleural mesothelioma: A population-based autopsy study. *J. Toxicol. Environ. Health Part A* **2016**, *79*, 129–141. [CrossRef]

63. Cangiotti, M.; Salucci, S.; Battistelli, M.; Falcieri, E.; Mattioli, M.; Giordani, M.; Ottaviani, M.F. EPR, TEM and cell viability study of asbestiform zeolite fibers in cell media. *Colloids Surf. B Biointerfaces* **2018**, *161*, 147–155. [CrossRef]

64. Pacella, A.; Cremisini, C.; Nardi, E.; Montereali, M.R.; Pettiti, I.; Giordani, M.; Mattioli, M.; Ballirano, P. Different erionite species bind iron into the structure: A potential explanation for fibrous erionite toxicity. *Minerals* **2018**, *8*, 36. [CrossRef]

65. Giordani, M.; Meli, M.A.; Roselli, C.; Betti, M.; Peruzzi, F.; Taussi, M.; Valentini, L.; Fagiolino, I.; Mattioli, M. Could soluble minerals be hazardous to human health? Evidence from fibrous epsomite. *Environ. Res.* **2022**, *206*, 112579. [CrossRef]

66. Gonda, I.; El Khalik, A.A.F. On the calculation of aerodynamic diameters of fibers. *Aerosol Sci. Technol.* **1985**, *4*, 233–238. [CrossRef]

67. Heyder, J.; Gebhart, J.; Rudolf, G.; Schiller, C.F.; Stahlhofen, W. Deposition of particles in the human respiratory tract in the size range 0.005–15 µm. *J. Aerosol Sci.* **1986**, *17*, 811–825. [CrossRef]

68. Pacella, A.; Ballirano, P.; Cametti, G. Quantitative chemical analysis of erionite fibres using a micro-analytical SEM-EDX method. *Eur. J. Mineral.* **2016**, *28*, 257–264. [CrossRef]

69. Campbell, L.S.; Charnock, J.; Dyer, A.; Hillier, S.; Chenery, S.; Stoppa, F.; Henderson, C.M.B.; Walcott, R.; Rumsey, M. Determination of zeolite-group mineral compositions by electron probe microanalysis. *Mineral. Mag.* **2016**, *80*, 781–807. [CrossRef]

70. Passaglia, E. The Crystal Chemistry of Chabazites. *Am. Mineral.* **1970**, *55*, 1278–1301.

71. Bruker, A.X.S. *Topas V.4.2: General Profile and Structure Analysis Software for Powder Diffraction Data*; Bruker AXS: Karlsruhe, Germany, 2009.

72. Cheary, R.W.; Coelho, A. A fundamental parameters approach to X-ray line-profile fitting. *J. Appl. Crystallogr.* **1992**, *25*, 109–121. [CrossRef]

73. Järvinen, M. Application of symmetrized harmonics expansion to correction of the preferred orientation effect. *J. Appl. Crystallogr.* **1993**, *26*, 525–531. [CrossRef]

74. Sabine, T.M.; Hunter, B.A.; Sabine, W.R.; Ball, C.J. Analytical expressions for the transmission factor and peak shift in absorbing cylindrical specimens. *J. Appl. Crystallogr.* **1998**, *31*, 47–51. [CrossRef]

75. Ballirano, P. Effects of the choice of different ionization level for scattering curves and correction for small preferred orientation in Rietveld refinement: The $MgAl_2O_4$ test case. *J. Appl. Crystallogr.* **2003**, *36*, 1056–1061. [CrossRef]

76. World Health Organization (WHO). *Asbestos and Other Natural Mineral Fibers*; Environmental Health Criteria: Geneva, Switzerland, 1986; Volume 53, pp. 69–107.

77. Stanton, M.F.; Layard, M.; Tegeris, A.; Miller, E.; May, M.; Morgan, E.; Smith, A. Relation of particle dimension to carcinogenicity in amphibole asbestoses and other fibrous minerals. *J. Natl. Cancer Inst.* **1981**, *67*, 965–975.

78. Elsen, J.; King, G.S.D.; Mottier, W.J. Influence of temperature on the cation distribution in calcium mordenite. *J. Phys. Chem.* **1987**, *91*, 5800–5805. [CrossRef]

79. Martucci, A.; Sacerdoti, M.; Cruciani, G.; Dalconi, C. In situ time resolved synchrotron powder diffraction study of mordenite. *Eur. J. Mineral.* **2003**, *15*, 485–493. [CrossRef]

80. Lotti, P.; Gatta, G.D.; Mellini, M.; Liermann, H.P. High-pressure behavior of synthetic mordenite-Na: An in situ single-crystal synchrotron X-ray diffraction study. *Z. Für Krist.* **2015**, *230*, 201–211. [CrossRef]

81. Mortier, W.J.; Pluth, J.J.; Smith, J.V. Positions of cations and molecules in zeolites with the mordenite-type framework, III: Rehydrated Ca-exchanged ptilolite. *Mater. Res. Bull.* **1976**, *11*, 15–22. [CrossRef]

82. Jones, J.B. Al-O and Si-O tetrahedral distances in aluminosilicate framework structures. *Acta Crystallogr.* **1968**, *24*, 355–358. [CrossRef]

83. Le Page, Y.; Donnay, G. Refinement of the crystal structure of low-quartz. *Acta Crystallogr.* **1976**, *B32*, 2456–2459. [CrossRef]

84. Young, R.A. *The Rietveld Method*; Young, R.A., Ed.; Oxford University Press: Oxford, UK, 1993.

85. Mortier, W.J. Compilation of extra framework sites in zeolites. Zeolites special issue. *Acta Cryst.* **1982**, *B38*, 2986.

86. Alberti, A. Location of Brønsted sites in mordenite. *Zeolites* **1997**, *19*, 411–415. [CrossRef]
87. Alberti, A.; Gottardi, G.; Lai, T. The determination of (Si,Al) distribution in zeolites. In *Guidelines for Mastering the Properties of Molecular Sieves*; Barthomeuf, D., Derouane, E.G., Hölderich, W., Eds.; NATO ASI Series, Series B: Physics; Plenum: New York, NY, USA, 1990; Volume 221, pp. 145–156.
88. European Committee for Standardization (CEN). *Workplace Atmospheres—Size Fraction Definitions for Measurement of Airborne Particles*; Report BS EN 481; British Standards Institute: London, UK, 1993.
89. Hartman, R.L.; Fogler, H.S. Understanding the dissolution of zeolites. *Langmuir* **2007**, *23*, 5477–5484. [CrossRef] [PubMed]
90. Gualtieri, A.F.; Andreozzi, G.B.; Tomatis, M.; Turci, F. Iron from a geochemical viewpoint. Understanding toxicity/pathogenicity mechanisms in iron-bearing minerals with a special attention to mineral fibers. *Free. Radic. Biol. Med.* **2019**, *133*, 21–37. [CrossRef]
91. Pascal, L.E.; Tessier, D.M. Cytotoxicity of chromium and manganese to lung epithelial cells in vitro. *Toxicol. Lett.* **2004**, *147*, 143–151. [CrossRef]
92. Gualtieri, A.F. Towards a quantitative model to predict the toxicity/pathogenicity potential of mineral fibers. *Toxicol. Appl. Pharmacol.* **2018**, *361*, 89–98. [CrossRef]
93. Wylie, A.; Korchevskiy, A. Epidemiology holds a key to the validation of toxicological models for elongate mineral particles. *Curr. Res. Toxicol.* **2022**, *3*, 100062. [CrossRef]